An Approach Towards Extreme Fast Charging Station Power Delivery for Electric Vehicles with Partial Power Processing

Vishnu Mahadeva Iyer, *Student Member, IEEE*, Srinivas Gulur, *Student Member, IEEE*, Ghanshyamsinh Gohil, *Member, IEEE*, and Subhashish Bhattacharya, *Senior Member, IEEE*

***Abstract*—This article proposes an approach for realizing the power delivery scheme for an extreme fast charging (XFC) station that is meant to simultaneously charge multiple electric vehicles (EVs). A cascaded H-bridge converter is utilized to directly interface with the medium voltage grid while dual-active-bridge based soft-switched solid-state transformers are used to achieve galvanic isolation. The proposed approach eliminates redundant power conversion by making use of partial power rated dc–dc converters to charge the individual EVs. Partial power processing enables independent charging control over each EV, while processing only a fraction of the total battery charging power. Practical implementation schemes for the partial power charger unit are analyzed. A phase-shifted full-bridge converter-based charger is proposed. Design and control considerations for enabling multiple charging points are elucidated. Experimental results from a downscaled laboratory test-bed are provided to validate the control aspects, functionality, and effectiveness of the proposed XFC station power delivery scheme. With a downscaled partial power converter that is rated to handle only 27% of the battery power, an efficiency improvement of 0.6% at full-load and 1.6% at 50% load is demonstrated.**

***Index Terms*—Cascaded H-bridge (CHB) converter, dc fast charger, dc–dc power converters, dual active bridge (DAB), energy storage, fast charging station, partial power processing, phase-shifted full-bridge (PSFB), solid-state transformer (SST).**

I. Introduction

TRANSPORT sector accounts for about 23% of the global energy-related CO_2 emissions with an annual emissions growth rate of 2.5% between 2010 and 2015. Transportation electrification is expected to play a major role in decarbonizing transport sector. Superior performance, lower operating cost, reduced greenhouse gas emissions, improvement in the battery technology, and driving range, along with the reduction in the vehicle cost have led to significant increase in the adoption rate of battery electric vehicles (BEVs) and plug-in hybrid electric vehicles [1].

Analysis indicates that the lack of electric vehicle (EV) charging infrastructure and prolonged charging time can lead to driving range anxiety [2]. AC level 1 charging (<2 kW) or ac level 2 charging (>2 kW and <10 kW) is most frequently used in a residential or workplace setting. AC level 2 charging is also typically used at both private and public facilities. For longer commutes, dc fast charging (>20 kW and <120 kW) stations are being deployed [3]. However, the charging time of BEV with a dc fast charger is still significantly higher than the refill time of the equivalent internal combustion engine vehicle. Therefore, it is envisaged that an extreme fast charging (XFC) system (>300 kW) is required to alleviate range anxiety and enable the widespread adoption of long range EVs [4], [5].

The XFC system for a 300-mile range vehicle can cost up to $100 000 per system. In addition, it requires special equipment, installation procedures, permits, and costly maintenance warranties [6]. Therefore, such a system will be typically owned by commercial customers or EV manufacturers. Several XFC systems can be arranged together to form an XFC station. Since an XFC station constitutes multiple XFC systems, it presents an opportunity for the reduction of capital investment and operating costs to make it economically viable.

The common approach of realizing an XFC station is to have a centralized front-end converter (FEC) unit that interfaces with the medium voltage (MV) grid using a line frequency transformer as shown in Fig. 1(a) [7]–[10]. The weight, size, volume, and large footprint of the line frequency transformer are serious concerns, especially in urban areas where cost of land is high. A direct MV grid interfaced fast charging station that utilizes a modular multilevel cascaded H-bridge (CHB) based FEC is reported in [5]. Dedicated full-rated dc–dc converter units are used for realizing the battery charging stage of the XFC system in all these approaches.

In this article, a novel power delivery architecture for an XFC station based on partial power charging units (PPCUs) is proposed and is depicted in Fig. 1(b). The CHB-based front-end and the solid-state transformers (SST) units are retained from [5]. Unlike in [5], the proposed solution offers a common low-voltage dc link, which can interface with local dc microgrids

Manuscript received February 18, 2019; revised May 17, 2019 and August 1, 2019; accepted September 15, 2019. Date of publication October 18, 2019; date of current version June 3, 2020. *(Corresponding author: Vishnu Mahadeva Iyer.)*

V. M. Iyer, S. Gulur, and S. Bhattacharya are with the NSF FREEDM Systems Center, North Carolina State University, Raleigh, NC 27695 USA (e-mail: vmahade@ncsu.edu; sgulur@ncsu.edu; sbhatta4@ncsu.edu).

G. Gohil is with the Electrical and Computer Science Engineering Department, University of Texas at Dallas, Richardson, TX 75080 USA (e-mail: ghanshyam.gohil@utdallas.edu).

Color versions of one or more of the figures in this article are available online at http://ieeexplore.ieee.org.

Digital Object Identifier 10.1109/TIE.2019.2945264

This work is licensed under a Creative Commons Attribution 4.0 License. For more information, see https://creativecommons.org/licenses/by/4.0/

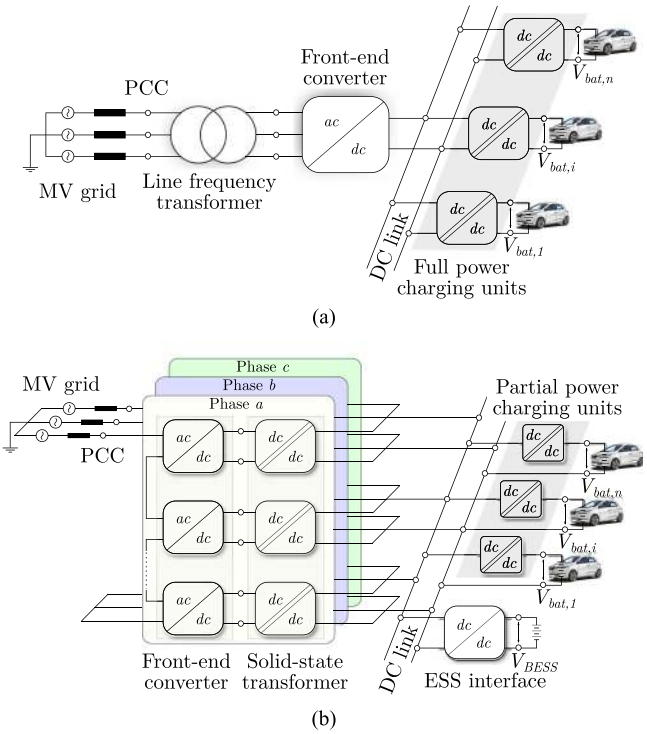

Fig. 1. XFC station architecture. (a) Conventional scheme with full rated charging converters. (b) Proposed scheme with partial rated charging converters.

such as a building-based microgrid. In order to reduce stress on the grid infrastructure and to avoid excess demand charges, centralized energy storage, and on-site energy generation can be integrated to the common dc link. The power rating of the CHB and SST units can be significantly reduced with such local energy storage solutions.

The novelty of the proposed scheme lies in the use of dc–dc converters that employ partial power processing for each charging point as against the full power dc–dc converter-based charging solution reported in the literature. The charging units are rated only to handle a fraction of the power required for battery charging. This approach can potentially reduce the installation and operational costs in an XFC station and simultaneously improve the overall system efficiency.

In the literature, partial power processing is also referred to as differential power processing [11]. A partial power converter is configured as a series element or a parallel element with the load that processes only a fraction of the total power [12]. The terminal connection configuration of a traditional power converter is typically modified to emulate it as a partial power processing element. Partial power processing converters have been successfully used to enhance the system performance in a variety of applications such as photovoltaic panel integration [12]–[14], thermoelectric generation systems [15], [16], datacenter power delivery schemes [17], and EV battery charging systems [18], [19]. Partial power processing based XFC station concept has been proposed in the conference version of this article [18]. In this article, the concept has been expanded and treated in a systematic manner with extensive system level analysis and cell

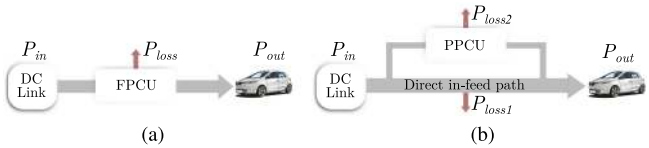

Fig. 2. Representative power flow diagram. (a) FPCU. (b) Series-pass PPCU.

level experimental validation. The specific contributions of this article are listed as follows:

1) Unidirectional, series-type partial power conversion schemes suited for extreme fast battery charging application are elucidated, and their performance compared. The system level benefits of using a partial power conversion scheme are analyzed (see Section II).
2) A practical, PPCU is conceptualized and its design considerations are discussed (see Section III).
3) Modeling and control considerations of the PPCU are discussed and a control strategy suited for battery charging is proposed (see Section IV).
4) Experimental results obtained from a hardware prototype developed in the laboratory are presented to showcase the functionality, control aspects and effectiveness of the proposed approach (see Section V).

II. Partial Power Charging Unit

As opposed to a conventional charging unit that processes the full power delivered to the EV battery as shown in Fig. 2(a), the PPCU processes only a fraction of that power, as shown in Fig. 2(b). Bulk power is transferred to the EV battery through a direct infeed path.

The PPCU enables battery charging at a controlled rate and can be envisaged as an active series-pass element that is used to interface the EV to the XFC station dc link. The desired operational features of the PPCU are listed as follows.

1) The PPCU should facilitate power transfer from the dc link to the EV battery at a controlled rate without consuming any power.
2) The PPCU should not introduce any circulating current between two or more charging points.
3) The PPCU should meet ripple voltage and current specifications as recommended by IEC 61851-23:2014 [20].

Such a PPCU can be practically realized using a traditional two-port dc–dc power converter. Any one port of the PPCU gets connected in series with the EV battery such that the voltage difference between the dc link and the EV battery is impressed upon it. The power processed by the converter is regenerated by connecting the other port of the PPCU to either the dc link or the EV battery. An isolated dc–dc converter topology is typically employed to facilitate regeneration. Past literature discusses several partial power converter realizations. However, a generic treatment, in terms of the various connection schemes to realize the partial power converter, is missing.

Universal schemes for realizing a series-pass PPCU are listed in Table I. Without loss of generality, it is assumed that power flows from Port 1 to Port 2 in the PPCU. All of these schemes

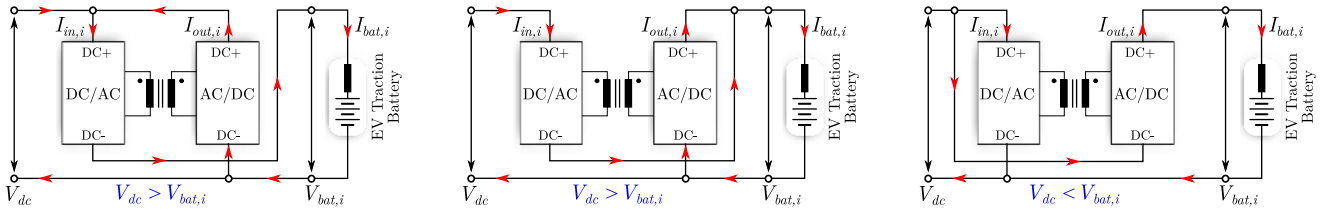

Fig. 3. Feasible partial power charger unit implementation schemes based on unidirectional isolated dc–dc converters that utilizes unidirectional voltage blocking switches. (a) Scheme 1 ($V_{dc} > V_{bat,i}$). (b) Scheme 2 ($V_{dc} > V_{bat,i}$). (c) Scheme 3 ($V_{dc} < V_{bat,i}$).

TABLE I
UNIVERSAL SCHEMES FOR PPCU REALIZATION

DC Voltage - Port 1 $V_{in,i}$	DC Voltage - Port 2 $V_{out,i}$	Feasibility for battery charging
$V_{dc} - V_{bat,i}$	V_{dc}	Yes
$V_{bat,i} - V_{dc}$	V_{dc}	No
$V_{dc} - V_{bat,i}$	$V_{bat,i}$	Yes
$V_{bat,i} - V_{dc}$	$V_{bat,i}$	No
V_{dc}	$V_{dc} - V_{bat,i}$	No
V_{dc}	$V_{bat,i} - V_{dc}$	Yes
$V_{bat,i}$	$V_{dc} - V_{bat,i}$	No
$V_{bat,i}$	$V_{bat,i} - V_{dc}$	No

Note: Without loss of generality, it is assumed that power flows from Port 1 to Port 2 in the PPCU.

may not be suitable for a battery charging application and need to be further examined. The following constraints are imposed to downselect the configurations suited for battery charging.

1) Reverse power flow from EV battery (vehicle-to-grid or V2G operation) is not considered.
2) Unidirectional voltage blocking switches are used for realizing the PPCU.

Since the proposed versatile XFC station has a central BESS unit that can be used to support advanced features, such as grid frequency regulation and peak shaving, there may not be much merit in incorporating V2G feature. Additionally, the XFC station will be typically owned by commercial customers and V2G may not be required. Hence, unidirectional charging converters are considered in this article. An additional physical constraint is imposed by the semiconductor choice for the PPCU. The dc voltage seen at any port has to be positive to ensure reliable operation of the PPCU as the selected semiconductors (in this case, silicon carbide (SiC) MOSFETs and Si diodes) can only block unidirectional voltages. Out of the eight universal schemes listed in Table I, there are only three feasible schemes that can be used for a dedicated battery charging application. The feasible schemes are depicted in Fig. 3. Feasibility is dictated by the power flow direction constraint in a PPCU. Solutions that are listed as infeasible in Table I will violate the first constraint as they drain power from the EV battery instead of charging it.

A. PPCU Performance Metrics

Let $V_{\text{out},i}$ and $I_{\text{out},i}$ denote the voltages and currents at the output port of the ith charging unit, $V_{\text{in},i}$ and $I_{\text{in},i}$ denote the voltages and currents at the input port of the ith charging unit, $V_{\text{bat},i}$ and $I_{\text{bat},i}$ denote the voltages and currents of the ith EV battery as indicated in Fig. 3. The instantaneous power demanded by the ith EV battery, $P_{\text{bat},i}(t)$ is given by

$$P_{\text{bat},i}(t) = V_{\text{bat},i}(t) I_{\text{bat},i}(t). \tag{1}$$

The instantaneous power at the input and output ports of the charging unit are given by

$$P_{\text{in},i}(t) = V_{\text{in},i}(t) I_{\text{in},i}(t) \tag{2}$$

$$P_{\text{out},i}(t) = V_{\text{out},i}(t) I_{\text{out},i}(t). \tag{3}$$

The expressions for voltages at the input and output ports of the charging unit are given in Table II. Furthermore, the battery current can be expressed in terms of the input and output port currents of the charging unit as follows:

$$I_{\text{bat},i}(t) = \begin{cases} I_{\text{in},i} \ (\text{Scheme 1}) \\ I_{\text{in},i} + I_{\text{out},i} \ (\text{Scheme 2}) \\ I_{\text{out},i} \ (\text{Scheme 3 and conventional scheme}) \end{cases}. \tag{4}$$

Let η_i refer to the efficiency of ith charging unit. By invoking power balance relationship ($P_{\text{out},i} = \eta_i P_{\text{in},i}$), the expressions for input and output port currents can be established as in Table II. Let partiality ratio, K_i denote the ratio of power processed by ith charging unit to the power transferred to the ith EV battery

$$K_i = P_{\text{in},i} / P_{\text{bat},i}. \tag{5}$$

A lower value of K_i will ensure a very high efficiency for the charger stage. However, practical constraints (such as the permissible swing on the dc bus voltage) exist that may limit the minimum K_i value achievable and is discussed later in Section III. Key converter parameters for assessing the performance of the charging unit are summarized in Table II. In practical PPCUs based on dc–dc converters with galvanic isolation, a nonactive power circulation is inevitable at the ac ports in addition to the desired active power flow [14]. The nonactive circulating power could degrade the performance of the PPCU in terms of additional losses within the converter. This has to be accounted during the topology selection as well as the design of the PPCU and is covered in Section III.

B. System Level Benefits

To showcase the system level benefits with the proposed approach, a case study for a multimegawatt XFC station with six charging points, each rated at 350 kW, is considered. It is assumed that the station is capable of simultaneously charging up

TABLE II
PARAMETERS FOR iTH CHARGING POINT FOR THE PPCU SCHEMES IN Fig. 3

	$V_{out,i}$	$V_{in,i}$	$I_{out,i}$	$I_{in,i}$	K_i	Comments
Conventional Scheme	$V_{bat,i}$	V_{dc}	$I_{bat,i}$	$\frac{V_{bat,i}I_{bat,i}}{\eta_i V_{dc}}$	$\frac{1}{\eta_i}$	Fixed input voltage, variable output voltage
PPCU Scheme 1	V_{dc}	$V_{dc}-V_{bat,i}$	$\frac{\eta_i I_{bat,i}(V_{dc}-V_{bat,i})}{V_{dc}}$	$I_{bat,i}$	$\frac{V_{dc}-V_{bat,i}}{V_{bat,i}}$	Variable input voltage, fixed output voltage
PPCU Scheme 2	$V_{bat,i}$	$V_{dc}-V_{bat,i}$	$\frac{\eta_i I_{bat,i}(V_{dc}-V_{bat,i})}{(1-\eta_i)V_{bat,i}+\eta V_{dc}}$	$\frac{I_{bat,i}V_{bat,i}}{(1-\eta_i)V_{bat,i}+\eta_i V_{dc}}$	$\frac{V_{dc}-V_{bat,i}}{(1-\eta_i)V_{bat,i}+\eta_i V_{dc}}$	Variable input voltage, variable output voltage
PPCU Scheme 3	$V_{bat,i}-V_{dc}$	V_{dc}	$I_{bat,i}$	$\frac{I_{bat,i}(V_{bat,i}-V_{dc})}{\eta_i V_{dc}}$	$\frac{V_{bat,i}-V_{dc}}{\eta_i V_{bat,i}}$	Fixed input voltage, variable output voltage

TABLE III
SYSTEM LEVEL CASE-STUDY TO SHOWCASE BENEFITS OF PROPOSED PPCU-BASED POWER DELIVERY SCHEME

Parameter	Conventional Scheme	PPCU Scheme 1	PPCU Scheme 2	PPCU Scheme 3
DC Link Voltage, V_{dc}	800 V	875 V	875 V	650 V
Total Charger Peak Power, $\sum_{i=1}^{6} max(P_{in,i})$	2.02 MW	0.36 MW	0.30 MW	0.38 MW
Cumulative Energy Loss per XFC Cycle, $\sum_{i=1}^{6} E_{loss,i}$	13.00 kWh	1.64 kWh	1.45 kWh	2.06 kWh
Cumulative Average Power Loss per XFC Cycle, $P_{loss-avg}$	78.04 kW	9.86 kW	8.71 kW	12.36 kW
Charger Efficiency, $\eta_{charger}$	95.0%	99.3%	99.4%	99.2%

Assumptions: 1) Efficiency, η of each converter (both full power and partial power) is assumed to be 95% at all operating points during one XFC cycle that lasts for 10 minutes. 2) A CC charging pattern with a charging current of 400 A is assumed as shown in Fig. 4(a).

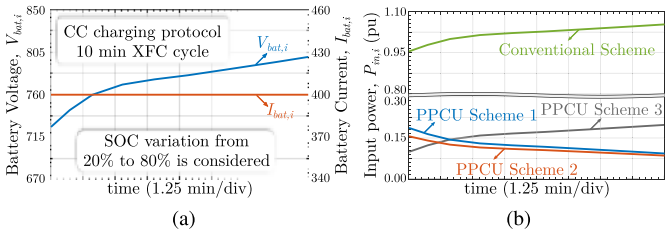

Fig. 4. (a) 10 min XFC cycle based on CC charging scheme. (b) Power plots of ith charging unit over an XFC cycle.

to 6 EVs. Currently, there is a trend to move toward 800 V dc system in passenger vehicles to facilitate XFC [21], [22] and hence, such a system is considered for this analysis. Although several techniques have been proposed for the high power charging mode in XFC systems, a representative, constant-current (CC), 10 min charge cycle presented in Fig. 4(a) is utilized for this article. The minimum battery pack voltage (725 V) corresponds to around 20% state of charge (SoC) while the maximum battery pack voltage (800 V) corresponds to around 80% SoC based on the LNMCO/graphite lithium ion (Li-ion) cell data provided in [23]. In fast charging systems, battery charging is stopped around 80% SoC to eliminate the time consuming, low power, constant-voltage (CV) charging mode.

Power processed by a charging unit over one XFC charge cycle for different charging schemes are evaluated based on Table II and plotted in Fig. 4(b). One full XFC charge cycle refers to the worst-case operation where 6 EVs are simultaneously getting charged for a duration of 10 min. Typical ratings of a conventional XFC station with six charging points are given in Table III.

The total energy transferred to the ith EV battery over one charging cycle, $E_{\text{bat},i}$ can be expressed as

$$E_{\text{bat},i} = \int_0^{T_{\text{cycle}}} P_{\text{bat},i}(t)dt \tag{6}$$

where T_{cycle} is the charging time corresponding to one XFC cycle. The instantaneous power loss in the ith charging unit can be expressed as

$$P_{\text{loss},i}(t) = (1-\eta_i)P_{\text{in},i}(t). \tag{7}$$

Since power processed by the partial rated charging unit is much lower than that of the conventional full rated charging unit, the absolute value of the losses is significantly less even with the same charging unit efficiency. The extra energy needed to meet the losses in the ith charging unit over one full charging cycle can be evaluated as

$$E_{\text{loss},i} = \int_0^{T_{\text{cycle}}} P_{\text{loss},i}(t)dt. \tag{8}$$

The cumulative average power loss in all the charging units over one XFC cycle can be computed as

$$P_{\text{loss-avg}} = \sum_{i=1}^{6} \frac{E_{\text{loss},i}}{T_{\text{cycle}}} \tag{9}$$

where $E_{\text{loss},i}$ is computed based on (8) in kWh. Finally, the efficiency of the charging stage can be computed as

$$\eta_{\text{charger}} = \frac{\sum_{i=1}^{6} P_{\text{bat},i}}{\sum_{i=1}^{6} P_{\text{bat},i} + P_{\text{loss-avg}}}. \tag{10}$$

Performance parameters are computed for the example system and quantified in Table III. The charger efficiency improves from 95 to $>$ 99% by adopting partial power charging converters. A 6

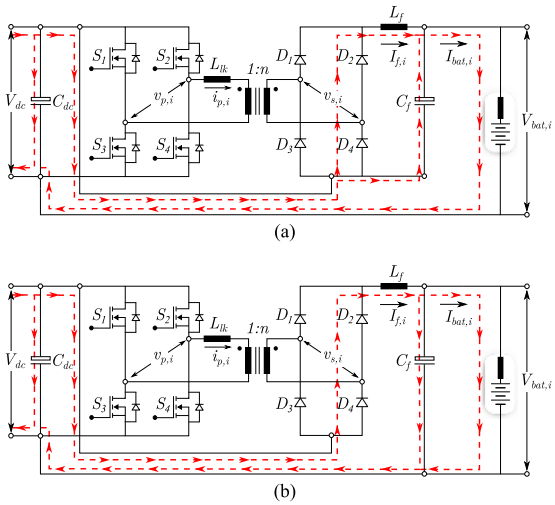

Fig. 5. Switching ripple propagation path (indicated by red dashed lines) in PPCU. (a) Typical filtering configuration. (b) Proposed filtering configuration.

TABLE IV
DC EV CHARGING STATION BATTERY CURRENT RIPPLE LIMITS

Limit, I_{lim}	Frequency
1.5 A	below 10 Hz
6 A	below 5 kHz
9 A	below 150 kHz

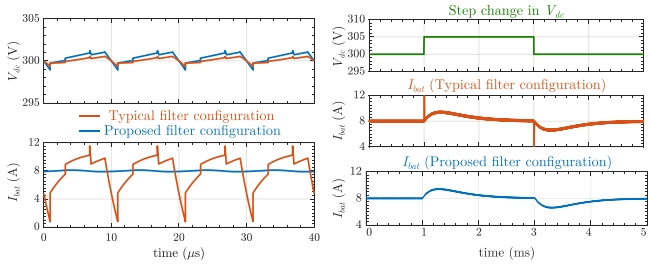

Fig. 6. Simulation results. (a) PPCU fed from an SST stage—Switching frequency ripple propagation effect. (b) PPCU fed from an ideal voltage source—disturbance propagation effect.

to 8 fold reduction can be achieved in the average power loss as well as the extra energy that needs to be expended to meet this loss over a charging cycle. The advantages with the proposed scheme are given as follows.

1) Lower rated charging units can lead to reduced capital costs.
2) Reduced energy requirements can result in lower operational costs.
3) Lower power rating of the charger and reduced losses can potentially enable power dense converter solutions as compared to conventional full rated charging units.

III. PPCU Realization and Design Considerations

A fixed frequency, zero voltage switched, modified PSFB pulsewidth modulation (PWM) converter topology shown in Fig. 5(b) is chosen as the PPCU candidate. Scheme 3 based terminal connection configuration is chosen as an example. The PSFB-PWM converter is popularly used in high power industrial systems [24] and is a scalable solution to suit XFC application.

The primary H-bridge legs of the PSFB-PWM converter are operated with a phase-shift, ϕ with respect to each other to achieve power transfer. Leg 1 (formed by S_1, S_3) is termed as the lagging leg and leg 2 (formed by S_2, S_4) is termed as the leading leg as the pole voltage (voltage between the output of any leg and the mid potential point of the input dc supply) of leg 2 leads that of leg 1. For details on the operation of PSFB-PWM converter, the interested reader is referred to [25]. The design considerations for the PSFB-PWM converter-based PPCU are listed as follows.

A. Disturbance Propagation and Filtering Arrangement

The typical output filter connection configuration of the PSFB-PWM converter shown in Fig. 5(a) is modified such that the filter capacitor, C_f appears in parallel with the EV battery as in Fig. 5(b). In the typical filtering configuration, there exists a low impedance path for the switching frequency ripple from the SST stage to directly propagate to the EV battery through the filter capacitor, C_f. Furthermore, any disturbance at the input dc link will propagate to the output through this low-impedance path. The proposed filtering configuration offers a true second-order filtering for the switching frequency ripple component.

To showcase the benefits of proposed filtering scheme, a circuit simulation is performed where the PPCU is fed from a dual-active-bridge (DAB) converter-based SST stage. Both the DAB stage and PPCU stage are switched at 50 kHz. The circuit parameters of the PPCU stage for this simulation are provided in Table V. The ripple component in battery current is plotted with the two filter configurations in Fig. 6(a). The presence of a low-impedance path through the output filter accentuates ripple propagation with the typical filter configuration.

Furthermore, in another simulation, the PPCU is fed from an ideal voltage source and a step voltage disturbance is introduced at the input dc link. The circuit parameters for this simulation are provided in Table V. The corresponding battery currents are plotted in Fig. 6(b). Current spikes are observed with the typical filtering configuration as a result of the low impedance path. The proposed filtering scheme attenuates the disturbance as expected.

B. Output Filter Design

The PPCU switching ripple current (peak to peak) in the filter inductor, L_f can be calculated as

$$\Delta I_{f,i} = \frac{\left[nV_{\text{dc}} - (V_{\text{bat},i} - V_{\text{dc}})\right] D_{\text{eff},i} T_s}{L_f} \tag{11}$$

where $V_{\text{bat},i}$ refers to the voltage of ith battery, $D_{\text{eff},i}$ refers to the effective duty cycle of the ith PPCU as defined in (22), and T_s refers to the switching period of PPCU.

The peak to peak current ripple limit, I_{lim} for a dc fast charging station as per IEC 61851-23:2014 is specified in Table IV. The

TABLE V
CHARGING UNIT CIRCUIT PARAMETERS

Parameter	PPCU	FPCU
DC link voltage, V_{dc}	300 V	425 V
Leakage Inductance, L_{lk}	3.5 μH	1.7 μH
Transformer turns ratio, n	0.35	1.0
Filter inductance, L_f	520 μH	520 μH
Filter capacitance, C_f	20 μF	20 μF
Snubber capacitance, C_{sn}	47 nF	47 nF
Snubber resistance, R_{sn}	500 Ω	2250 Ω
Switching frequency, f_{sw}	50 kHz	50 kHz
EV Battery voltage, V_{bat}	$360-400$ V	$360-400$ V
Battery peak power, P_{bat}	3.2 kW	3.2 kW

output filter should be designed such that $\Delta I_{f,i} \leq I_{\text{lim}}$ based on (11).

C. Partiality Ratio, K_i

The partiality ratio, K_i of the PSFB-PWM converter shown in Fig. 5(b) decreases with a higher dc bus voltage, which in-turn will improve the system efficiency

$$K_i = \frac{V_{\text{bat},i} - V_{\text{dc}}}{\eta_i V_{\text{bat},i}}. \tag{12}$$

However, the selection of an appropriate input dc bus voltage, V_{dc} is closely linked to the reliable operation of the PPCU. For the chosen PPCU scheme (Scheme 3), the maximum dc bus voltage, $V_{\text{dc-max}}$ is dictated by the minimum battery voltage, $V_{\text{bat},i-\text{min}}$

$$V_{\text{dc-max}} < V_{\text{bat},i-\text{min}}. \tag{13}$$

This is to ensure that the voltage at the output dc port ($V_{\text{out}} = V_{\text{dc}} - V_{\text{bat},i}$) always remains positive. If the steady-state value of dc bus voltage is chosen very close to $V_{\text{bat},i-\text{min}}$, there exists a possibility that (13) may be violated under transient conditions or in the presence of any disturbances. Hence, it is recommended that

$$V_{\text{dc}} = \frac{V_{\text{bat},i-\text{min}}}{(1+x)} \tag{14}$$

where x is a safety margin that is chosen based on the maximum permissible voltage swing in the dc bus voltage. This automatically imposes a constraint on the partiality ratio, K_i. The range of K_i as shown in (15) can be obtained by substituting the minimum and maximum values of battery voltage, $V_{\text{bat},i}$ and the expression for dc bus voltage, V_{dc} [from (14)] in (12)

$$\frac{x}{\eta_i(1+x)} \leq K_i \leq \frac{V_{\text{bat},i-\text{max}} - \frac{V_{\text{bat},i-\text{min}}}{1+x}}{\eta_i V_{\text{bat},i-\text{max}}} \tag{15}$$

In this article, a 20% safety margin ($x = 0.2$) is assumed.

D. Selection of Transformer Turns-Ratio

Minimum value of transformer turns ratio, n_{min} is limited by the maximum phase-shift, $\phi_{i,\text{max}}$ permissible in the PSFB-PWM converter [14]

$$n_{\text{min}} > \frac{V_{\text{bat},i-\text{max}} - V_{\text{dc}}}{D_{i,\text{max}} V_{\text{dc}}}, \quad D_{i,\text{max}} = \frac{\phi_{i,\text{max}}}{\pi} \tag{16}$$

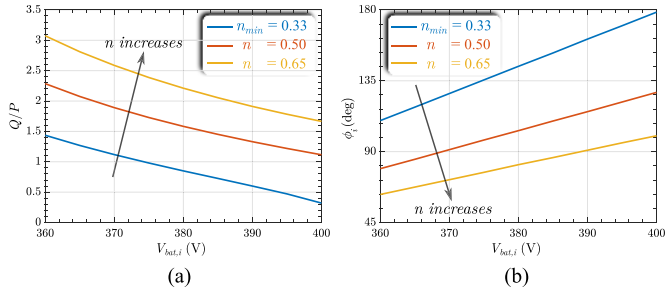

Fig. 7. Simulation plots. (a) Variation of Q/P ratio with battery voltage, $V_{i,\text{bat}}$. (b) Variation of operating phase-shift, ϕ with battery voltage, $V_{i,\text{bat}}$.

where $\phi_{i,\text{max}}$ is the maximum phase-shift angle in radians. The maximum permissible value of transformer-turns ratio, n_{max} is limited to minimize the impact of nonactive circulating power when the battery voltage varies over a wide range. The nonactive circulating power, Q is defined as

$$Q = \sqrt{S^2 - P^2} \tag{17}$$

where P refers to the active power handled by the converter and S refers to the apparent power as seen from the primary ac port. P and S are defined as

$$P = (V_{\text{bat},i} - V_{\text{dc}}) I_{\text{bat},i}\ , \quad S = v_{p,i-\text{rms}} i_{p,i-\text{rms}}. \tag{18}$$

As an example, the variation of Q/P ratio with battery voltage is plotted for different turns-ratio conditions in Fig. 7(a) and the corresponding variation in operating phase-shift, ϕ_i is plotted in Fig. 7(b). The battery voltage, input voltage, and other converter parameters (except turns-ratio as it is varied) are specified in Table V. It can be seen that the Q/P ratio is lowest when the turns-ratio, $n = n_{\text{min}}$. The turns-ratio should be chosen as close as possible to n_{min} to minimize the impact of nonactive circulating power. In reality, the turns-ratio should be chosen slightly higher than n_{min} to handle practical nonidealities such as deadtime and unaccounted voltage drops within the converter.

E. Zero Voltage Switching (ZVS) and Deadtime Selection

ZVS mechanism and deadtime selection considerations of PSFB-PWM converter have been reported in the literature and the interested reader is referred to [25] and [26] for further details. The selection of deadtime plays a critical role in achieving ZVS across a wide load range.

F. Voltage Overshoots and Snubber Design

In a PSFB-PWM converter, the leakage inductance, L_{lk} will ring with the parasitic output capacitance of the secondary bridge diodes. Passive or active snubbers are typically used to clamp the secondary voltage to a desired level. A bus-side RCD type snubber is implemented as in [24].

IV. MODELING AND CONTROL OF PPCU

Individual EV battery current control is achieved by regulating the output filter inductor current of the PFSB-PWM

converter based PPCU. The small-signal modeling aspects of PSFB-PWM converter have been extensively discussed in the literature [27]–[29]. The proposed terminal connection configuration of the PSFB-PWM converter [see Fig. 5(b)] to enable partial power processing may have an effect on the dynamic behavior of the converter. This needs to be examined for designing a robust and stable control system. The approach presented in [27], where the PSFB-PWM converter small-signal model is derived by incorporating duty cycle modulation effects within the model for a PWM buck converter, is used to extract the small-signal transfer functions for controller design.

A. Duty Cycle Modulation Effects

Leakage inductance, L_{lk} of the PSFB-PWM converter will affect the diode bridge commutation. A larger leakage inductance results in a duty cycle loss as it dictates the slope of the current waveform when a voltage is applied to the primary [27]. The loss in duty cycle, ΔD_i, for the ith PPCU can be expressed as in [25]

$$\Delta D_i = \frac{2nL_{lk}}{V_{\text{in},i}T_s}\left(2I_{f,i} - \frac{V_{\text{out},i}}{L_f}(1-D_i)\frac{T_s}{2}\right). \tag{19}$$

Based on the terminal connection configuration for a Scheme 3 based ith PPCU [see Fig. 3(c) and Table II],

$$V_{\text{in},i} = V_{\text{dc}},\ V_{\text{out},i} = V_{\text{bat},i} - V_{\text{dc}} \tag{20}$$

The converter is typically designed to operate in deep continuous conduction mode; hence, the term containing $(1-D_i)$ can be neglected [27]. Equation (19) can be simplified as

$$\Delta D_i \approx \frac{4nL_{lk}}{V_{\text{in},i}T_s}I_{f,i}. \tag{21}$$

The effective duty cycle, $D_{\text{eff},i}$ can now be computed as

$$D_{\text{eff},i} = D_i - \Delta D_i. \tag{22}$$

B. Small-Signal Model and Linearized Transfer Functions

To understand the impact of duty cycle modulation effects on the small-signal response, (22) is perturbed and linearized

$$\hat{d}_{\text{eff},i} = \hat{d}_i + \hat{v}_{\text{in},i}\left[\frac{4nL_{lk}I_{f,i}}{V_{\text{in},i}^2T_s}\right] - \hat{i}_{f,i}\left[\frac{4nL_{lk}}{V_{\text{in},i}T_s}\right] \tag{23}$$

where $\hat{v}_{\text{in},i} = \hat{v}_{\text{dc}}$.

This effective duty cycle perturbation can now be incorporated within the small-signal model for a PWM buck converter with the proposed terminal connection configuration. An interested reader is directed to [30] for the small-signal model derivation for a PWM buck converter. An unterminated, small-signal model for the PSFB-PWM converter that is fed from an ideal voltage source, V_{dc} is presented in Fig. 8. Small-signal open-loop impedance seen at the output port of ith PPCU can be expressed

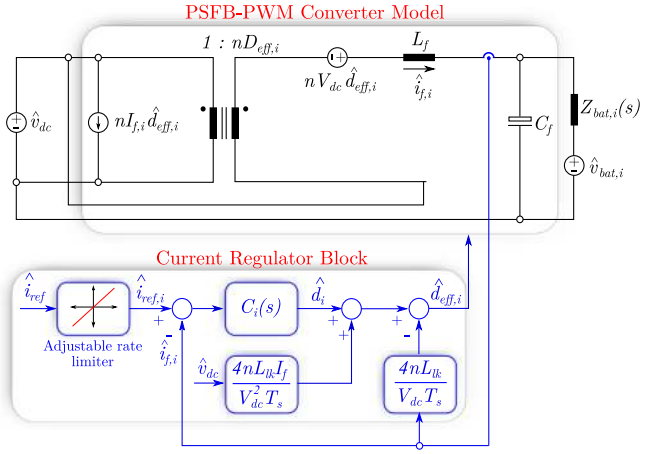

Fig. 8. Unterminated small-signal model of modified PSFB-PWM converter based ith PPCU with output current regulation. $Z_{\text{bat},i}(s)$ refers to battery internal impedance.

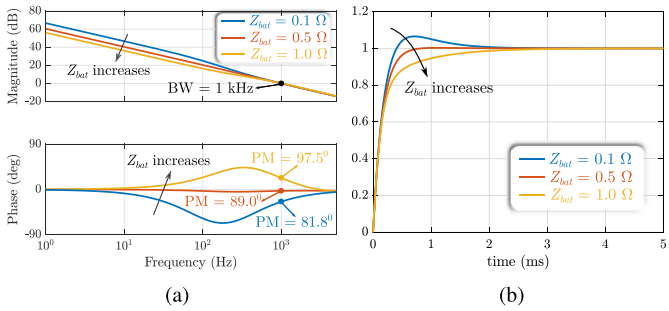

Fig. 9. Simulation plots. (a) Loop gain transfer function and stability margins. (b) Step response of closed-loop transfer function.

as

$$Z_{\text{out},i}(s) = Z_{\text{bat},i}(s)\left[\frac{1 + \frac{sL_f}{Z_{\text{bat},i}(s)} + s^2L_fC_f}{1 + sZ_{\text{bat},i}(s)C_f}\right]. \tag{24}$$

The small-signal transfer function relating the filter inductor current and effective duty ratio can now be extracted from the model

$$\left.\frac{\hat{i}_{f,i}(s)}{\hat{d}_{\text{eff},i}(s)}\right|_{\substack{\hat{v}_{\text{dc}}(s)=0\\ \hat{v}_{\text{bat},i}(s)=0}} = \frac{nV_{\text{dc}}}{Z_{\text{out},i}(s)}. \tag{25}$$

The control to output plant transfer function for the ith PPCU, $P_i(s)$ can now be evaluated from (23) to (25).

$$P_i(s) = \left.\frac{\hat{i}_{f,i}(s)}{\hat{d}_i(s)}\right|_{\substack{\hat{v}_{\text{dc}}(s)=0\\ \hat{v}_{\text{bat},i}(s)=0}} = \frac{nV_{\text{dc}}}{Z_{\text{out},i}(s) + \frac{4n^2L_{lk}}{T_s}}. \tag{26}$$

Comparing (26) with the results presented in [27], it can be discerned that the proposed terminal connection configuration does not affect the small-signal control to output dynamics of the unterminated PSFB-PWM converter based PPCU.

A proportional-integral (PI) type current regulator, $C_i(s)$ is designed to regulate the filter inductor current. The small-signal current-regulator implementation is depicted in Fig. 8. The loop

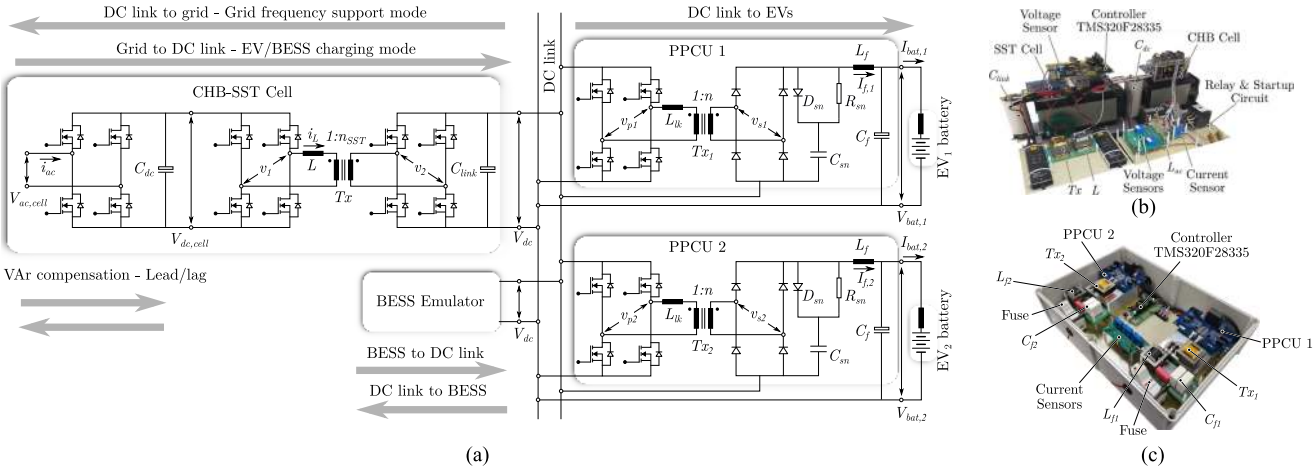

Fig. 10. Laboratory test-bed for the down-scaled XFC station with two charging points. A cell level realization of the ac–dc FEC and dc–dc solid-state transformer is implemented. (a) Circuit topology. (b) CHB-SST cell—hardware prototype. (c) PPCUs—hardware prototype.

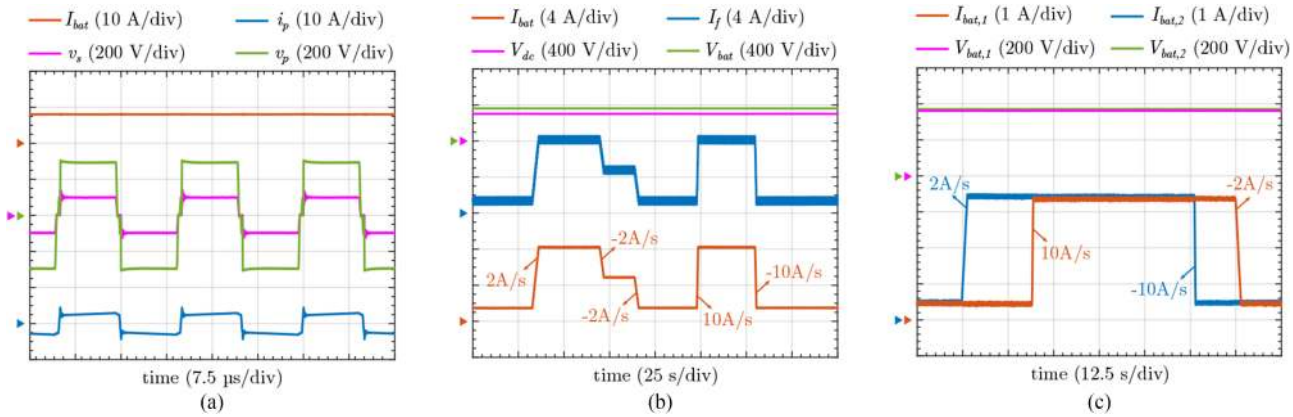

Fig. 11. Experimental waveforms from PPCU. (a) Standalone operation where 3.2 kW power is being delivered to the battery. (b) Closed-loop control of battery current. (c) Simultaneous operation of two closed-loop controlled PPCUs. The waveforms in (a) and (b) are labeled based on the circuit schematic shown in Fig. 5(b) and the waveforms in (c) are labeled based on the circuit schematic shown in Fig. 10(a).

gain, $L(s)$ and closed-loop transfer function, $T(s)$ are given by

$$L(s) = C_i(s)P_i(s),\ T(s) = \frac{C_i(s)P_i(s)}{1 + C_i(s)P_i(s)}. \tag{27}$$

Bode plots of the loop gain are plotted with different battery impedances in Fig. 9(a). The battery impedance is approximated as a resistance in the frequency range of interest (100 Hz to a few kHz). It can be seen that the bandwidth degradation is minimal when the battery impedance is varied over a wide range while the phase-margin slightly deteriorates with a decrease in battery impedance. The step response of the closed-loop transfer function is presented in Fig. 9(b). As expected, a slight overshoot is observed in the response as the battery impedance is decreased and this can be attributed to the lower phase-margin.

V. Results

A down-scaled hardware test-bed has been developed in the laboratory [shown in Fig. 10(a)] to validate the advantages of using partial power processing in XFC architecture. The relevant electrical and circuit parameters of the same are listed in Table V. For the CHB-SST-based front-end, a single cell has been realized and tested. A DAB converter is used to implement the SST cell. Two partial power charger units based on the PSFB-PWM converter have been interfaced to the SST cell dc link. A dc power supply is interfaced to the SST cell dc link to emulate the role of a central BESS. Electronic load banks are used as CV sources to emulate the characteristics of EV batteries. Extensive experimental results are presented in Figs. 11–16 to validate the feasibility and functionality of the proposed approach.

The steady-state operation of the PPCUs are investigated in Fig. 11. The operating waveforms for a single standalone PSFB-PWM converter based PPCU when it delivers around 3.2 kW of active power to the battery are shown in Fig. 11(a). In Fig. 11(b), the battery current is being regulated by the PPCU as per the proposed control approach discussed in Section IV. An adjustable slope based ramp feature is incorporated wherein the EV battery current can be ramped at a controlled rate to any desired value as demanded by the EV. The provision of such a ramp feature is recommended in IEC 61851-23:2014. Fig. 11(c)

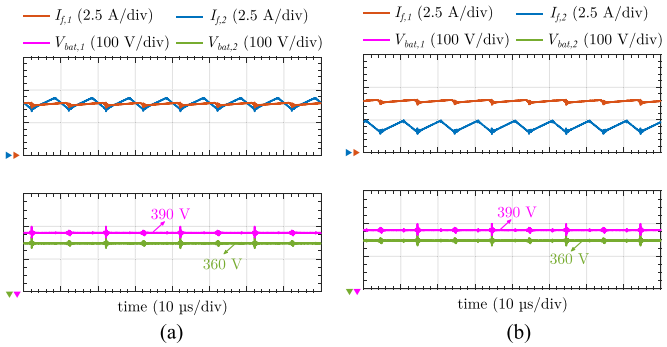

Fig. 12. Steady-state experimental waveforms of PPCUs. (a) Same charging current, different battery voltage levels. (b) Different battery currents, different battery voltage levels. The waveforms are labeled based on the circuit schematic in Fig. 10(a).

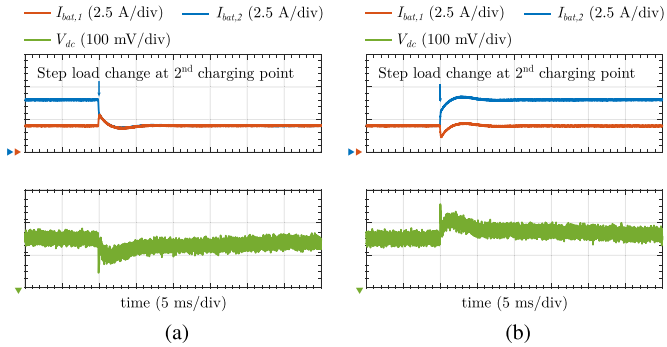

Fig. 13. Experimental plots showcasing the coupling effects between battery currents. (a) Step reference change of -2 A is introduced in $I_{f,2}$. (b) Step reference change of $+2$ A is introduced in $I_{f,2}$.

demonstrates simultaneous and independent charging of two EV batteries by two PPCUs with different ramp rates (e.g., 10 A/s and 2 A/s for PPCU 1 and 2, respectively, during a positive ramp slope).

The proposed partial power based charging units have been integrated with the CHB-SST cell and the corresponding experimental results are presented in Fig. 12. In this battery charging test, 1.5 kW of power is supplied from the grid and the rest ($\approx$ 1.5 kW) is supplied by the central BESS. Each PPCU transfers a power of around 1.5 kW to the respective EV battery while processing only a fraction of the same. The dc bus voltage, V_{dc} is regulated to 300 V by the CHB-SST cell. The two PPCUs connected to the output bus of the SST cell are individually responsible for charging their respective EV batteries in current regulated mode achieved using PI controllers. Fig. 12(a) and (b) outline two charging cases (with similar and different output inductor currents) when the battery voltages ($V_{\text{bat},1} = 390$ V and $V_{\text{bat},2} = 360$ V) are different for both the EVs. This demonstrates the system level operation as well as the capability of the proposed approach to handle different battery voltages and operating power at different charging ports.

Since the inputs of the PPCUs are connected to the same dc link (output of the SST cell), there exists a coupling between the PPCU output battery currents. To understand the coupling effect between the battery currents of both the PPCUs, a step reference change of $\pm$ 2 A in $I_{f,2}$ is created as seen in Fig. 13(a) and (b). It is observed that when a step reference change is initiated in $I_{f,2}$, the common dc bus undergoes a sudden change in voltage ($\approx$ 120 mV) that correspondingly creates a disturbance in $I_{f,1}$ and in $I_{\text{bat},1}$ ($\approx$ 1 A). As observed from both Fig. 13(a) and (b), the robustness of the feedback control system helps $I_{f,2}$ and $I_{f,1}$ to track their respective references and reject any external disturbances.

To validate efficiency benefits, the proposed PPCU [see Fig. 5(b)] is compared with a conventional full power charging unit (FPCU). The PSFB-PWM converter based realization of the FPCU is given in Fig. 14. The circuit parameters for the FPCU and the PPCU are given in Table V. The experimental power losses of the FPCU and the PPCU are compared in Fig. 15(a) while Fig. 15(b) compares the charger efficiencies

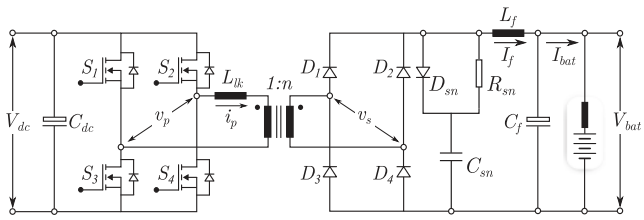

Fig. 14. FPCU implementation.

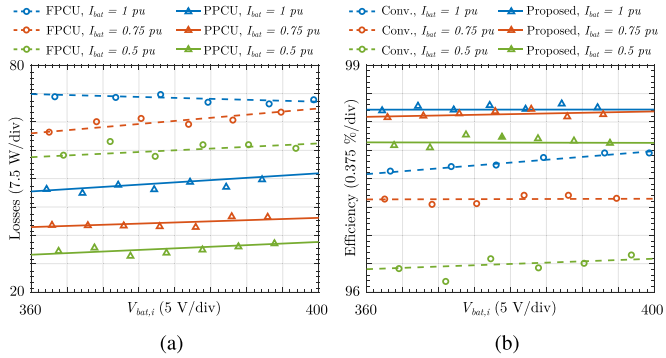

Fig. 15. Experimental plots. (a) Power loss comparison of full power and PPCUs. (b) Efficiency comparison of conventional (FPCU based) and proposed (PPCU based) charger schemes. 1 p.u. (per unit) of current corresponds to 8 A. Yokogawa WT3000 precision power analyzer is used for measurements.

of the proposed scheme (PPCU based) with the conventional scheme (FPCU based). The EV battery is charged in CC mode for this set of tests and the results are presented for different values of battery current to understand performance implications under part-load conditions. The benefits of the proposed scheme, in terms of efficiency improvement, is better under both part-load and full-load conditions. At full-load ($P_{\text{bat}} = 3.2$ kW, $V_{\text{bat}} = 400$ V) condition, the losses in the PPCU are 27% lower than that in the FPCU. Hence, at this operating point, the efficiency of the proposed scheme is about 0.6% higher than the conventional scheme. At 50% loading condition, an efficiency improvement of 1.6% is obtained with the proposed scheme over a conventional scheme.

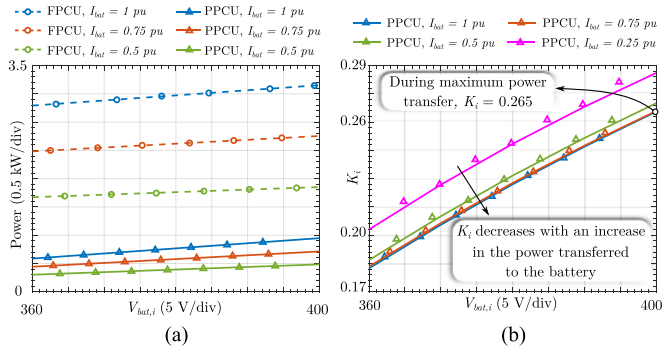

Fig. 16. Experimental plots. (a) Input power comparison of full power and PPCUs. (b) Partiality ratio, K_i. 1 p.u. (per unit) of current corresponds to 8 A. Yokogawa WT3000 precision power analyzer is used for measurements.

TABLE VI
COMPARISON OF ELECTRICAL STRESSES IN PPCU AND FPCU

Parameter	PPCU	FPCU
VA Rating of Inductor, L_f ($V_{rms}I_{rms}$)	0.125 pu	0.38 pu
VA Rating of Transformer, Tx ($V_{rms}I_{rms}$)	0.24 pu	1.04 pu
Stress in MOSFETs, $S_1 - S_4$ ($V_{pk}I_{rms}$)	0.18 pu	0.71 pu
Stress in Diodes, $D_1 - D_4$ ($V_{pk}I_{rms}$)	0.24 pu	1.00 pu

Note: Worst case VA rating or switch stress is compared. Base current (8 A) and base voltage (400 V) are chosen based on the maximum battery current and voltage respectively.

The power rating of a PPCU is compared with that of an FPCU across different load conditions as shown in Fig. 16(a). It is discerned that the PPCU power rating at full-load ($P_{\text{bat}} = 3.2$ kW, $V_{\text{bat}} = 400$ V) is only about 27% as compared to that of the FPCU. The partiality ratio, is computed based on the experimental data and plotted in 16(b). The partiality ratio tends to deteriorate at light-load conditions. This is attributed to the deterioration in PSFB-PWM converter efficiency at light-loads due to loss of ZVS as well as the undesired nonactive circulating power. However, this will not impact the rating of the PPCU as the absolute active power handled by the converter is lower under light load conditions. At the maximum power transfer condition ($P_{\text{bat}} = 3.2$ kW, $V_{\text{bat}} = 400$ V), the value of K_i is 0.265 and is indicative of the power rating of the PPCU. Furthermore, the electrical stresses seen by active and passive components of both PPCU and FPCU are compared in Table VI. It can be seen that the active and passive components are subjected to a much lower electrical stress ($\approx$ 25–30%) in a PPCU as expected.

VI. CONCLUSION

An approach toward a power delivery architecture for an XFC station that makes use of multiple PPCUs was proposed in this article. System level benefits of using the proposed power delivery scheme include lower capital investments, lower operational costs, and improved power and energy efficiency. The features and requirements of using such a PPCU for a battery charging application were discussed and a suitable converter topology was identified for the same. Design, modeling, and control considerations of the PPCU, specific to electric vehicle battery charging, were discussed and analyzed. Experimental results from a down-scaled laboratory test-bed validated the control aspects, functionality, and effectiveness of the proposed power delivery scheme. With the down-scaled prototypes, it was demonstrated that the PPCU that was rated to handle only 27% of the battery power provided an efficiency improvement of 0.6% at full load (3.2 kW) and 1.6% at 50% load (1.6 kW) as compared to an FPCU that was rated to handle the full battery power.

The XFC power delivery scheme, though quite promising, still needs to overcome various adoption and technical challenges for commercial viability. Although each charging port is galvanically isolated from the grid, the proposed partial power charger based power delivery scheme does not offer any galvanic isolation between the individual charging ports. IEC 61851-23:2014 standard on dc charging stations states that "Requirements for multiple simultaneous outputs, which are nonisolated from each other, are under consideration. It is of the hope that promising nonisolated solutions (such as the solution presented in this article) could potentially influence standards organizations to come up with appropriate regulations." Furthermore, state-of-the-art commercial fast charging systems, such as the 120-kW TESLA supercharger, charge an 80-kWh Li-ion-based battery close to 1.5 C (C refers to charging rate or C-rate). 350-kW XFC systems would charge such a battery at around 4.4 C. Charging at such high C-rates can lead to lithium plating which, in turn, results in accelerated degradation of the battery. The efficiency of the battery at around 5 C is only around 88–93% [31]. This calls for improved thermal management solutions combined with next generation battery management systems to enable XFC for ensuring safe and reliable operation of the battery. Some of the other challenges in moving toward XFC stations include modification of existing standards and identification of a sustainable business model. Aspects such as fault handling and protection, safety, standardization of EV charging equipment, interoperability requirements, and communication protocols need to be addressed.

REFERENCES

[1] "Global EV outlook 2017," International Energy Agency, 2017. Accessed: Nov. 27, 2017. [Online]. Available: https://www.iea.org/publications/freepublications/publication/GlobalEVOutlook2017.pdf
[2] L. Dickerman and J. Harrison, "A new car, a new grid," *IEEE Power Energy Mag.*, vol. 8, no. 2, pp. 55–61, Mar./Apr. 2010.
[3] D. Karner, T. Garetson, and J. Francfort, "EV charging infrastructure roadmap," Idaho National Laboratory, 2016. Accessed: Nov. 27, 2017. [Online]. Available: https://avt.inl.gov/sites/default/files/pdf/evse/EVChargingInfrastructure RoadmapPlanning.pdf
[4] D. Aggeler *et al.*, "Ultra-fast DC-charge infrastructures for EV-mobility and future smart grids," in *Proc. IEEE PES Innovative Smart Grid Technol. Conf. Eur.*, Oct. 2010, pp. 1–8.
[5] M. Vasiladiotis and A. Rufer, "A modular multiport power electronic transformer with integrated split battery energy storage for versatile ultrafast EV charging stations," *IEEE Trans. Ind. Electron.*, vol. 62, no. 5, pp. 3213–3222, May 2015.

[6] *Evaluating Electric Vehicle Charging Impacts and Customer Charging Behaviors—Experiences From Six Smart Grid Investment Grant Projects*, Smart Grid Investment Grant Program, U.S. Department of Energy, Washington, DC, USA, Dec. 2017.
[7] *Considerations for Corridor and Community DC Fast Charging Complex System Design*, U.S. Department of Energy, Washington, DC, USA, May 2017, pp. 1–51.
[8] S. Bai and S. M. Lukic, "Unified active filter and energy storage system for an MW electric vehicle charging station," *IEEE Trans. Power Electron.*, vol. 28, no. 12, pp. 5793–5803, Dec. 2013.
[9] S. Rivera, B. Wu, S. Kouro, V. Yaramasu, and J. Wang, "Electric vehicle charging station using a neutral point clamped converter with bipolar DC bus," *IEEE Trans. Ind. Electron.*, vol. 62, no. 4, pp. 1999–2009, Apr. 2015.
[10] J. C. G. Justino, T. M. Parreiras, and B. J. C. Filho, "Hundreds kW charging stations for e-buses operating under regular ultra-fast charging," *IEEE Trans. Ind. Appl.*, vol. 52, no. 2, pp. 1766–1774, Mar./Apr. 2016.
[11] P. S. Shenoy and P. T. Krein, "Differential power processing for DC systems," *IEEE Trans. Power Electron.*, vol. 28, no. 4, pp. 1795–1806, Apr. 2013.
[12] M. Kasper, D. Bortis, and J. W. Kolar, "Classification and comparative evaluation of PV panel-integrated DC–DC converter concepts," *IEEE Trans. Power Electron.*, vol. 29, no. 5, pp. 2511–2526, May 2014.
[13] H. Zhou, J. Zhao, and Y. Han, "PV balancers: Concept, architectures, and realization," *IEEE Trans. Power Electron.*, vol. 30, no. 7, pp. 3479–3487, Jul. 2015.
[14] J. R. R. Zientarski, M. L. d. S. Martins, J. R. Pinheiro, and H. L. Hey, "Series-connected partial-power converters applied to PV systems: A design approach based on step-up/down voltage regulation range," *IEEE Trans. Power Electron.*, vol. 33, no. 9, pp. 7622–7633, Sep. 2018.
[15] A. Petucco, S. Saggini, L. Corradini, and P. Mattavelli, "Analysis of power processing architectures for thermoelectric energy harvesting," *IEEE J. Emerg. Sel. Topics Power Electron.*, vol. 4, no. 3, pp. 1036–1049, Sep. 2016.
[16] K. Sun, Z. Qiu, H. Wu, and Y. Xing, "Evaluation on high-efficiency thermoelectric generation systems based on differential power processing," *IEEE Trans. Ind. Electron.*, vol. 65, no. 1, pp. 699–708, Jan. 2018.
[17] E. Candan, P. S. Shenoy, and R. C. N. Pilawa-Podgurski, "A series-stacked power delivery architecture with isolated differential power conversion for data centers," *IEEE Trans. Power Electron.*, vol. 31, no. 5, pp. 3690–3703, May 2016.
[18] V. M. Iyer, S. Gulur, G. Gohil, and S. Bhattacharya, "Extreme fast charging station architecture for electric vehicles with partial power processing," in *Proc. IEEE Appl. Power Electron. Conf. Expo.*, 2018, pp. 659–665.
[19] J. Rojas, H. Renaudineau, S. Kouro, and S. Rivera, "Partial power DC–DC converter for electric vehicle fast charging stations," in *Proc. 43rd Annu. Conf. IEEE Ind. Electron. Soc.*, 2017, pp. 5274–5279.
[20] *Electric Vehicle Conductive Charging System—Part 23: DC Electric Vehicle Charging Station*, IEC Standard 61851-23:2014, Mar. 2014.
[21] C. Jung, "Power up with 800-V systems: The benefits of upgrading voltage power for battery-electric passenger vehicles," *IEEE Electrific. Mag.*, vol. 5, no. 1, pp. 53–58, Mar. 2017.
[22] "Tribute to tomorrow. Porsche Concept Study Mission E," Porsche, Accessed: Nov. 27, 2017. [Online]. Available: https://www.porsche.com/microsite/mission-e/international.aspx
[23] C. Zhang, J. Jiang, L. Zhang, S. Liu, L. Wang, and P. C. Loh, "A generalized SOC-OCV model for lithium-ion batteries and the SOC estimation for LNMCO battery," *Energies*, vol. 9, no. 11, 2016. [Online]. Available: http://www.mdpi.com/1996-1073/9/11/900
[24] J. N. Ganesh, K. Viswanathan, R. Naik, M. Rose, J. Sabate, and Y. V. Singh, "High frequency power distribution unit (HFPDU) for MRI systems," in *Proc. 19th Eur. Conf. Power Electron. Appl.*, Sep. 2017, pp. P.1–P.7.
[25] J. A. Sabate, V. Vlatkovic, R. B. Ridley, F. C. Lee, and B. H. Cho, "Design considerations for high-voltage high-power full-bridge zero-voltage-switched PWM converter," in *Proc. 5th Annu. Proc. Appl. Power Electron. Conf. Expo.*, 1990, pp. 275–284.
[26] L. Zhao, H. Li, Y. Hou, and Y. Yu, "Operation analysis of a phase-shifted full-bridge converter during the dead-time interval," *IET Power Electron.*, vol. 9, no. 9, pp. 1777–1783, 2016.
[27] V. Vlatkovic, J. A. Sabate, R. B. Ridley, F. C. Lee, and B. H. Cho, "Small-signal analysis of the phase-shifted PWM converter," *IEEE Trans. Power Electron.*, vol. 7, no. 1, pp. 128–135, Jan. 1992.
[28] M. J. Schutten and D. A. Torrey, "Improved small-signal analysis for the phase-shifted PWM power converter," *IEEE Trans. Power Electron.*, vol. 18, no. 2, pp. 659–669, Mar. 2003.
[29] G. D. Capua, S. A. Shirsavar, M. A. Hallworth, and N. Femia, "An enhanced model for small-signal analysis of the phase-shifted full-bridge converter," *IEEE Trans. Power Electron.*, vol. 30, no. 3, pp. 1567–1576, Mar. 2015.
[30] R. W. Erickson and D. Maksimovic, *Fundamentals of Power Electronics*, 2nd ed. Norwell, MA, USA: Kluwer, 2004.
[31] D. Sauer *et al.*, "Challenges for battery system and battery management designs for highly reliable & ultra-fast charging applications," 04 2019, doi: 10.13140/RG.2.2.22596.68486.

Vishnu Mahadeva Iyer (S'16) received the B.Tech. degree in electrical and electronics engineering from the College of Engineering, Trivandrum, Trivandrum, India, in 2011, and the M.E. degree in electrical engineering from the Indian Institute of Science (IISc), Bengaluru, Bengaluru, India, in 2013. He is currently working toward the Ph.D. degree in electrical and computer engineering with the NSF FREEDM Systems Center, NC State University, Raleigh, NC, USA.

He was a Power Electronics Engineer with GE Global Research Center, Bengaluru, India, from 2013 to 2015. His current research interests include power electronics for automotive applications, grid-connected power converters, resonant and soft-switched power converters, control and stability of power electronic systems, etc.

Srinivas Gulur (S'16) received the B.E. degree in electrical and electronics engineering from Anna University, Chennai, India, in 2010, and the M.S. degree in electrical engineering systems from the University of Michigan, Ann Arbor, MI, USA, in 2013. He is currently working toward the Ph.D. degree in electrical and computer engineering with the NSF FREEDM Systems Center, North Carolina State University, Raleigh, NC, USA.

He worked with the Power Electronics Group, Indian Institute of Science (IISc), Bengaluru, Bengaluru, India, from 2013 to 2015. His current research interests include modeling and advanced control of grid-connected power converters and electromagnetic interference (EMI) modeling, and mitigation schemes for power electronic converters.

Ghanshyamsinh Gohil (S'13–M'16) received the M.Tech. degree in electrical engineering with specialization in power electronics and power systems from the Indian Institute of Technology Bombay, Mumbai, India, in 2011, and the Ph.D. degree in electrical engineering from the Department of Energy Technology, Aalborg University, Denmark, in 2016.

He is currently an Assistant Professor of Department of Electrical and Computer Engineering with the University of Texas at Dallas, Richardson, TX, USA. He was a Postdoctoral Researcher with the FREEDM Systems Center, North Carolina State University, Raleigh, NC, USA, where his focus was on the combined photovoltaic (PV)-energy storage system and medium voltage power conversion. Before joining Ph.D., he was a Lead Research Engineer with the Siemens Corporate Technology and a Deputy Manager Technology with the Crompton Greaves Global R&D Center, where he worked on the MicroGrid, PV inverter, and power quality issues. His research interests include wide bandgap power semiconductor devices, medium voltage power conversion, smart energy systems, electric vehicle technologies, parallel operation of voltage-source converters, and the design of the inductive power components.

Subhashish Bhattacharya (M'85–SM'13) received the B.E. degree from the Indian Institute of Technology—Roorkee, Roorkee, India, the M.E. degree from the Indian Institute of Science, Bengaluru, India, and the Ph.D. degree from the University of Wisconsin-Madison, Madison, WI, USA, in 2003, all in electrical engineering.

He was with the FACTS and Power Quality Division, Westinghouse/Siemens Power T&D, during 1998 to 2005. In August 2005, he joined North Carolina State University, Raleigh, NC, USA, where he is currently the Duke Energy Distinguished Professor in Electrical and Computer Engineering. He is a founding Faculty Member of NSF FREEDM Systems Center and DOE Power America Institute. A part of his Ph.D. research on active power filters was commercialized by York Corporation for air-conditioner chillers. His research interests include solid-state transformers, medium voltage power converters, FACTS, utility applications, high-frequency magnetics, and power conversion applications of silicon carbide devices.